The carbon cycle and the COVID-19 lock-down

J. S. Reid[1]

[1]Independent Researcher, 33 Charlotte St., New Norfolk, Tas. 7140, Australia

Key Points:

- The effect of CO_2 emissions decrease during the COVID lock-down is masked by natural variations in mixed layer temperature such as El Niño.
- The precise exponential decay of ^{14}C concentration following the cessation of nuclear weapons testing indicates diffusion of CO_2 from the atmosphere into a larger reservoir such as the deep ocean.
- The Impulse Response Function statistically estimated from observed CO_2 emission and concentration time series is exponential with no significant fraction retained by the atmosphere.

Corresponding author: John Reid, johnsinclairreid@gmail.com

Abstract

Two unintended experiments provide insight into the role of anthropogenic emissions in the ocean-atmosphere carbon cycle. One was the temporary reduction in emissions during the COVID-19 lock-down. The other was the emission of a radioactive isotope of carbon during the testing of nuclear weapons in the 1950s and the abrupt cessation of these tests in 1963. Together they imply the existence of two distinct reservoirs which exchange carbon with the atmosphere, viz.: the mixed layer and the deep ocean. Exchanges with the former are noisy because they are influenced by sea surface temperature which, in turn, depends on weather events such as El Nino. They completely mask any variations caused by the COVID-19 lock-down. Exchanges with the deep ocean are steady, long-term and uninfluenced by the weather. The long term relationship between CO2 concentration due to variations in CO2 emissions is summarised by the Impulse Response Function. This can estimated from observed time series using the ARX method augmented by testing residuals for self-correlation. It was found to be a simple exponential with a half-time of 43 years with no remnant component. The longer half times and large remnant fraction of the impulse response derived from ocean circulation models is attributed to the failure of these models to properly account for turbulent mixing in the deep ocean.

1 Introduction

Before the COVID-19 pandemic of 2020, emissions of carbon dioxide were rising by about one percent per year over the previous decade. Government policies during the COVID-19 pandemic changed patterns of energy demand around the world due to reduced transport and changed consumption patterns. This short, unexpected and random variation in emissions and the response of the global carbon system to this sudden fall in production rate may yield insights into the mechanisms controlling the concentration of CO_2 in the atmosphere.

2 Inferences from Direct Observations

2.1 Carbon Dioxide Measurements

Daily global CO_2 emissions decreased by seventeen percent by early April 2020 compared with the mean 2019 levels. At their peak, emissions in individual countries decreased by 26 percent on average. At issue is whether this perturbation was detected by any of the atmospheric baseline monitoring stations around the world. Figure 1 shows data from two, the Cape Grim, Tasmania, Baseline Air Pollution Station, operated by CSIRO Marine and Atmospheric Research and the Australian Bureau of Meteorology, and the Mauna Loa Observatory in Hawaii (Keeling et al., 2009).

Let $\dot{m}$ be the rate of anthropogenic emissions of CO_2, then Figure 3b of Le Quéré et al. (2020) shows that the dip in $\dot{m}$, $\Delta\dot{m}$, during the first five months of 2020 to be about 15 Mt per day, i.e $15\times10^{-3}\times(365/12) = .45$ Pg/month. For a well-mixed atmosphere, the corresponding dip, $\Delta\dot{c}$, in the rate of change of concentration of CO_2, c, is given by

$$\Delta\dot{c} = \frac{\Delta\dot{m}}{M} \tag{1}$$

where $M = 5.15\times10^6$ Pg is the mass of the atmosphere. Substituting in (1) and multiplying by 10^6 to give parts per million yields $\Delta\dot{c} = .087$ ppm/month.

Values of $\dot{c}$ derived as the first differences of the monthly average concentration, c, measured at the Cape Grim and Mauna Loa observatories are shown in Figure 1a and Figure 1b respectively. Thirteen month running means are also shown. There is a significant linear trend in both time series. The standard deviations, σ, of the residuals were 0.14 and 0.30 ppm/month respectively. The dashed lines show the 2σ confidence limits above and below the trend lines. The expected fall in $\Delta\dot{c}$ of .087 ppm/month is thus

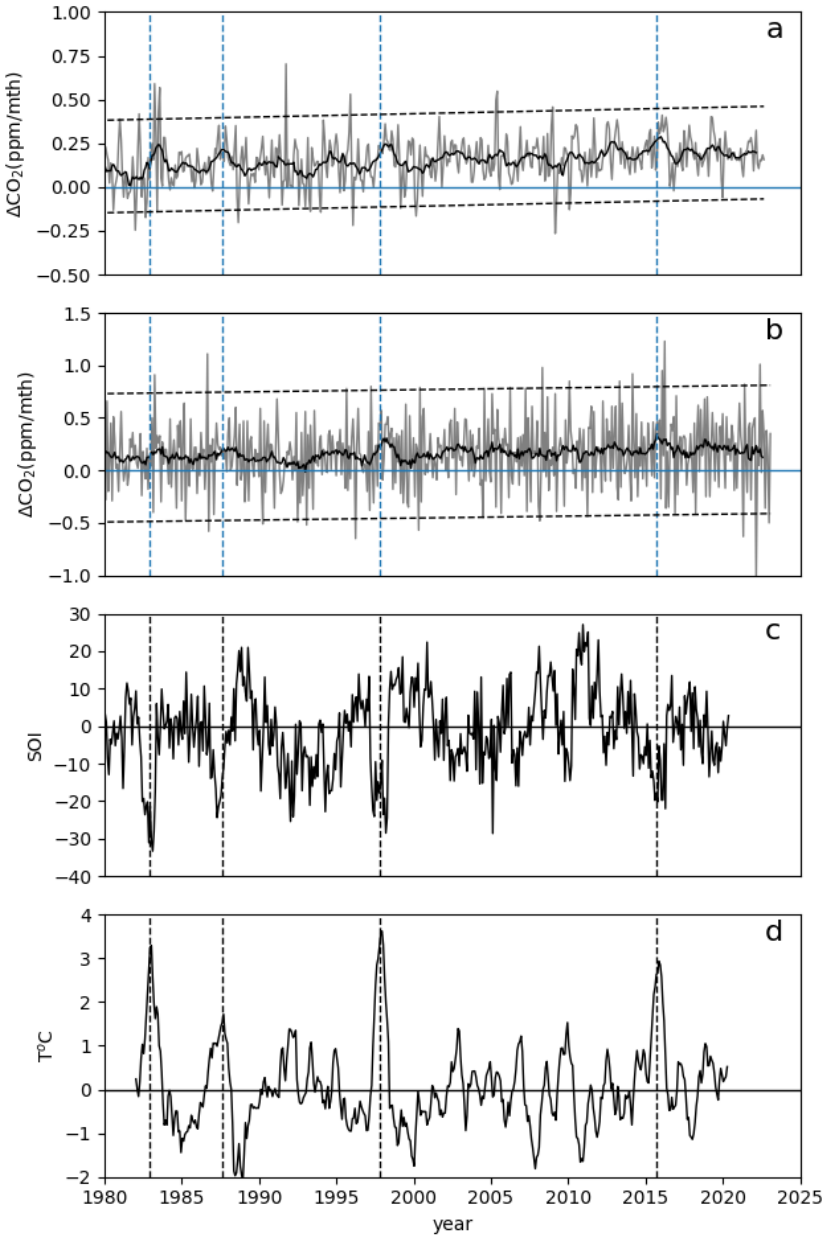

Figure 1. Monthly rate of change in atmospheric CO2 concentration (grey) and 13 month running mean (black) at Cape Grim (**a**) and Mauna Loa (**b**). Horizontal dashed lines show 2σ confidence limits. **c**. Southern Oscillation Index. **d**. Sea Surface Temperature anomaly of the Nino 3 region of the Equatorial Pacific. Vertical dashed lines are times of peak SST.

too small to be evident in the observations. On a time scale of months the COVID-19 lock-down event was masked by ongoing natural processes.

The two lower panels give an indication of what such natural processes might be. Figure 1c shows the Southern Oscillation Index for the period in question. The SOI is calculated from the sea level pressure difference between Tahiti and Darwin. Sustained negative excursions of the SOI are termed El Niño events and are associated with increases in Sea Surface Temperature in the Eastern Equatorial Pacific as shown in Figure 1d for the Niño3 region, 5°N-5°S, 150°W-90°W (Trenberth, 1997). The times of the SST peaks in Figure 1d are shown by vertical dashed lines in all four panels.

All four El Niño warming events are associated with increases in the running means of atmospheric CO_2 concentration at both Cape Grim and Mauna Loa. This is not surprising. The solubility of CO_2 in sea water is strongly dependent on temperature and it comes out of the ocean when SST increases. In general, the high frequency noisiness of the monthly differences can be accounted for by the degassing and absorption of CO_2 by the upper part of the ocean as it is heated and cooled by changing weather systems.

2.2 The Bomb Test Curve

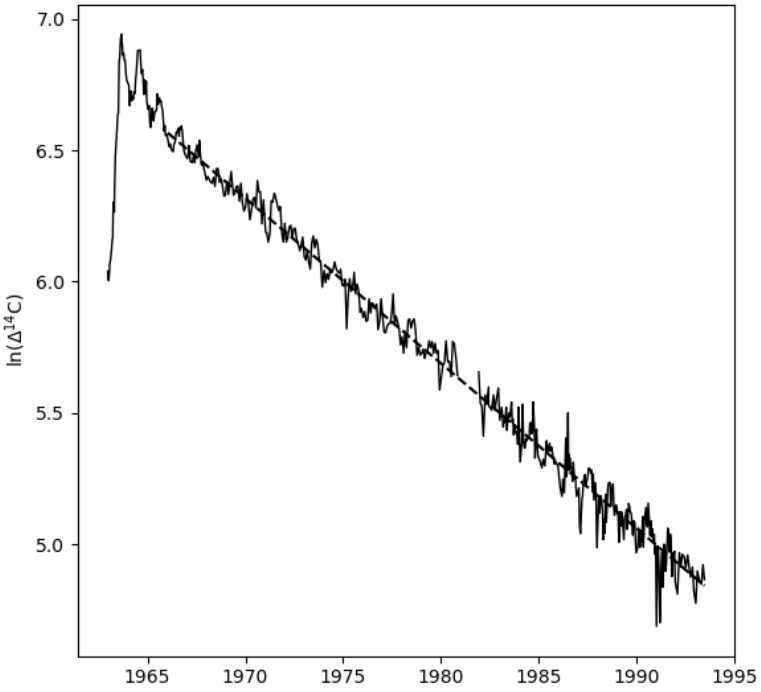

Figure 2. The natural logarithm of $\Delta^{14}C$ values recorded at Fruholmen, Norway as a function of timeDashed line: regression line fitted between January 1966 and June 1993.

.

The testing of nuclear weapons during the 1950s and 1960s injected significant amounts of the radioactive ^{14}C isotope of carbon into the atmosphere. More importantly, the abrupt

Statistic	Value
slope	-.06289
intercept	-7.76×10^{-15}
r	-0.9939
r^2	0.9878
standard error	.0003395

Table 1. Regression Statistics

cessation of atmospheric testing following the Nuclear Test Ban Treaty of 5 August 1963, meant that the rate of production of the ^{14}C isotope reverted to the constant natural background level. This allows the movement of carbon dioxide between natural reservoirs to be assessed in much the same way that radioactive isotopes are used to assess the rates of metabolic processes in nuclear medicine.

The decrease in Δ^{14}C is known as "The Bomb Test Curve". Numerous observations were made in the decades following the cessation of testing following the Nuclear Test Ban Treaty. Here we look at a single high quality data set from Fruholmen, Norway (Nydal and Lövseth, 1983) shown in Figure 2. The natural logarithm, $\ln(\Delta^{14}\mathrm{C})$, is plotted on the vertical axis rather than Δ^{14}C itself so that exponential behaviour becomes linear. A regression line was fitted between January 1966 and the end of the data set in June 1993.

Regression statistics are shown in Table 1. The fit is remarkably good and accounts for 98.8 percent of the variance. Hence, with a high degree of accuracy:

$$\Delta^{14}C = Ae^{-t/\tau} \tag{2}$$

where A is the value of Δ^{14}C at $t = 0$ and τ is the time constant given by $\tau = -1/\text{slope}=$ 15.9$\pm$0.085 years. The time for Δ^{14}C to decay to half its initial value is given by $t_{1/2} = -\tau\ln(0.5)= 11.02 \pm .059$ years.

Thus half of the bomb test $^{14}CO_2$ disappears from the atmosphere every 11 years. Equation (2) is the solution of the classic diffusion equation:

$$\frac{dc}{dt} + \frac{c}{\tau} = F(t) \tag{3}$$

where c is the concentration of the quantity being diffused ($\Delta^{14}CO_2$ in this case), τ is the diffusion time or time constant and $F(t)$ specifies the rate at which concentration increases due to new material being introduced into the reservoir. In this case following the cessation of nuclear testing $F(t)$ is the constant background rate associated with the bombardment of upper atmosphere Nitrogen by cosmic rays.

Carbon dioxide reacts with water to form carbonate and bicarbonate ions. Hence the diffusion rate of carbon *per se* involves reaction rates and diffusion rates for each of these three species. These are almost completely independent of atomic mass Zeebe (2011) and so all the isotopes of carbon, ^{12}C, ^{13}C, ^{14}C, in the form of CO_2 and its radicles, diffuse through water at the same rate and the time constant, τ, in (3) applies equally to all isotopic species of CO_2.

It is therefore reasonable to assume that CO_2 diffuses from the atmosphere into some other reservoir or sink. The excellent fit of a single regression line indicates that any diffusion process must be dominated by a single sink with a single time constant. Furthermore the fact that the atmospheric $\Delta^{14}CO_2$ has, by now, returned to its pre-bomb

Name	Symbol	Value
rate of change of concentration	dc/dt	13.9
concentration	c	2860
time constant	τ	15.9
anthropogenic production rate	$A(t)$	36.5

Table 2. Present day values of variables in equation (4) in units of $PgCO_2$/year.

background level implies that the sink is much larger than the source, the atmosphere. The only candidate sink which fulfils these conditions is the deepocean.

2.3 Upwelling and the Redfield ratios

Since the atmosphere is not depleted of CO_2 by this diffusion process, there must be some way in which CO_2 is returned to the atmosphere. This occurs in regions of upwelling where deep ocean water outcrops into the mixed layer. There are a number of such regions in the world. They are commonly associated with western boundary currents, high levels of primary production and rich fisheries.

At decadal time scales, equation (3) can be rewritten

$$\frac{dc}{dt} + \frac{c}{\tau} = A(t) + U(t) \tag{4}$$

where τ is the diffusion time evaluated above, A(t) is the anthropogenic production rate and U(t) is the production rate from deep ocean upwellings. Here c is the concentration of CO_2 in the atmosphere and mixed layer (assumed to be in equilibrium at these longer time scales). $U(t)$ can be evaluated in from the other terms in (4) listed in Table 2 giving $U(t) = 157$ $PgCO_2$/year.

The World Ocean Circulation Experiment (WOCE) aimed to establish the role of the World Ocean in the Earth's climate system. WOCE's field phase ran between 1990 and 1998, and was followed by an analysis and modelling phase that ran until 2002. Ganachaud and Wunsch (2000) used high resolution trans-oceanic section gathered during WOCE in an inverse model to improve estimates of the global circulation and heat flux. Here we use their estimate of upwelling in just one area of the ocean together with WOCE chemical data to demonstrate the scale of this mechanism.

The area chosen was the entire Atlantic between WOCE sections A02 (45° N) and A10 (30° S). It includes two major upwellings along its eastern land boundary. According to Figure 2 of Ganachaud and Wunsch, the total upwelling in this box is 10 ± 2.5 Sv.

Seemingly all that is needed for a rough estimate of the rate of CO_2 upwelling is to multiply this flux of seawater with the average concentration but this would overlook the the role of phytoplankton in removing CO_2 by photosynthesis when the up-welled nutrient is illuminated by sunlight. The Redfield ratio Redfield (1934) is the atomic ratio of carbon, nitrogen and phosphorus (C:N:P=106:16:1) found in marine phytoplankton. Thus in the up-welled water 106 atoms of carbon are removed for each 16 atoms of nitrogen. However the concentration of carbon in the deep Atlantic is well in excess of the Redfield ratio and it is the remaining fraction which ends up in the mixed layer and the atmosphere.

Visual examination of the WOCE Section A09 of the Atlanticshows a CO_2 concentration of around 2200 μmole/kg whereas that of Nitrate is generally less than about

23 μmole/kg. Multiplying the nitrate concentration by 106/16 and subtracting leaves 2050 μmole/kg of CO_2 in the mixed layer after phytoplankton has absorbed these nutrients. Other WOCE Atlantic sections show much the same concentrations of nitrogen, carbon and, hence, excess carbon as does this section, so that, within, say ten percent, this value pertains to the entire Atlantic Ocean below 1500m. Multiplying by the the upwelling rate gives a rate of upwelling of 76 Mt/day of CO_2 = 28 Pg/year of CO_2 = 7.6 Pg/year of carbon. These values are of the same order as the the anthropogenic emission rates quoted in Le Quéré et al. (2020). Given that this calculation included only the Atlantic Ocean, the global value of 157 Pg/year of CO_2 calculated in the previous section is not unreasonable.

3 A Statistical Approach

3.1 Estimating an Impulse Response Function

There is a further, more powerful method of gaining insight into the ocean-atmosphere carbon cycle. It is the regression method of frequentist statistics.

It is common practice across a wide range of sciences to treat physical quantities as ensemble parameters and to estimate them from sample statistics. A time series is a particularly type of sample, one in which a series of measurements are taken at equal intervals of time or averaged over equal intervals of time. The Pearson correlation coefficient is often used to describe the relationship between contemporaneous time series, but it is a poor statistic because it does not account for temporal ordering. Two other statistics, which better summarize the relationship between two concurrent time series, are the impulse response and the sensitivity. The impulse response is the response of the endogenous or dependant variable to a short pulse in the exogenous or independent variable. The sensitivity is defined here as the response of the endogenous variable to unit step-function in the exogenous variable. It is the sum of terms (or integral) of the impulse response.

Both statistics can be estimated using the "autoregressive with exogenous variable" or ARX method as shown in Appendix A. Their existence and the number of ARX regression coefficients required for their computation, is established by rejecting those configurations whose residuals show significant self-correlation. The impulse response is then found as the convolutional reciprocal of a sequence derived from the ARX regression coefficients. These ideas originated with Box and Jenkins (1976). Here we derive these statistics using convolutional methods and apply them to carbon cycle time series.

This approach makes no assumptions about the underlying physics, other than that the system under investigation is random, rather than deterministic, and that it is stationary and ergodic. It gives results which conflict with those based on numerical models. A more intuitive, physical approach is given by Dengler and Reid (2023).

3.2 The Model-Derived IRF

A normalized Impulse Response Function $\Im(t)$ was first derived using a global circulation model by Maier-Reimer and Hasselmann (1987) (MRH), viz:

$$\Im(t) = A_0 + \sum_{j=1}^{4} A_j \exp(-t/\tau_j) \tag{5}$$

Where the A_j are the proportions corresponding to various decay times, τ_j. A_0 is nonzero. The time constants, τ_j range from 1.2 years to 362.9 years. A very similar model, the HILDA model, was proposed by Siegenthaler and Joos (1992) which ultimately became the Bern model of the IPCC reports. The impulse response function, once known, is a great convenience for modellers because it allows atmospheric CO_2 concentration,

$y(x)$, to be determined for any arbitrary emission rate, $x(t)$, using the convolution

$$y(x) = \int \Im(t - t')x(t')dt' \tag{6}$$

where $x(t)$ has been scaled to have the same units as $y(t)$.

In order to assess the non-linear response of pCO_2 to total carbon in the mixed layer, MRH ran their model using three input emission scenarios comprising increases of (a) quadrupling, (b) doubling and (c) increasing by 1.25%, the initial atmospheric CO_2 concentration[1]. The three impulse response functions are shown in Figure 3. Values of A_0 were 0.131, 0.142 and 0.166 respectively which determine the remnant fractions of atmospheric CO_2 under the three scenarios.

There is something very odd about this. Certainly we might expect a remnant fraction to remain in the atmosphere once the oceanic reservoir is saturated. What is odd is that the three remnant fractions are almost the same. In each case, we would expect the reservoir to take up roughly the same *absolute* amount of CO_2 before it becomes saturated, in which case a much larger *fraction* would remain in the atmosphere in the quadrupling case than in the 25% increase case. This is not what happens to the dotted curves in Figure 3. The similarity of the remnant fractions in the three cases does not imply saturation. Rather, it implies a partitioning of the available CO_2 between two reservoirs with a volume ratio of the order of $(1 - r)/r$, where r is the remnant fraction. When we apply this to the MRH model, the oceanic reservoir into which atmospheric CO_2 is diffused has only about six times the CO_2 capacity of the atmosphere. Given that the ocean has been estimated to carry fifty times the steady-state, atmospheric load of CO_2 (Houghton et al., 2001), this is a remarkably small value. It implies that, in the MRH model, CO_2 is partitioned between the atmosphere and a small sub-reservoir from which little escapes into the remainder of the ocean.

3.3 The Observed IRF

The ARX method developed above was applied to annual means (Meinshausen et al., 2017) of atmospheric CO_2 concentration , C_i, vs global fossil fuel emissions, E_i. Global fossil fuel emissions for the interval 1850 to 2014, were downloaded from the Carbon Dioxide Information Analysis Center (Boden et al., 2017).

Applying the Ljung-Box test to the residuals given by (A3) for ARX(p) for $p = 0, ..., 5$ resulted in zero probabilities in all cases. The ARMAX method revealed a significant moving average component with $q = 2$. For this reason both time series were decimated by 2 and the ARX / Ljung-Box method reapplied. The results for the decimated data are shown in Table 3. The probability, P, for the ARX(1) run has a value of 0.4359 indicating that the null hypothesis that the residuals are unselfcorrelated cannot be rejected. Thus the simplest regression relationship between C_i and E_i which unambiguously fits the data is the ARX(1) model, viz.:

$$C_i = \hat{\alpha}_0 E_i + \hat{\alpha}_1 C_{i-1} \ , \ \ i = 1, ..., N \tag{7}$$

where the estimated regression coefficients are $\hat{\alpha}_0 = 0.21$ and $\hat{\alpha}_1 = 0.969$ with 95 percent confidence limits 0.945 and 0.992. The prediction error filter is $\{1, -\hat{\alpha}_1\}$ which has convolutional inverse $\{1, \hat{\alpha}_1, \hat{\alpha}_1^2, ...\}$, a geometric sequence with common ratio $\hat{\alpha}_1$. The nth term of the IRS estimate is given by

$$\hat{I}_n = \hat{\alpha}_0 \hat{\alpha}_1^n = \hat{\alpha}_0 \exp(-\frac{nq\Delta t}{\tau}) \tag{8}$$

[1] Their definition is slightly ambiguous. Their equation (5) defines it correctly but the accompanying text appears to define a "step response function".

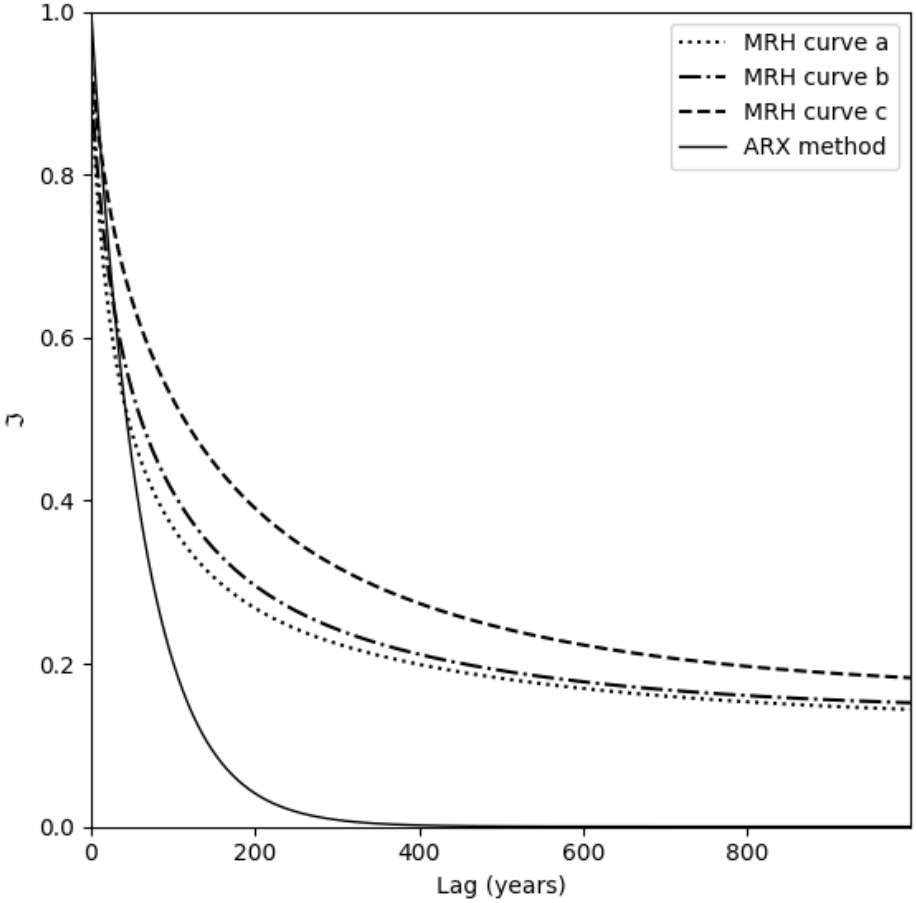

Figure 3. The normalized impulse response, $\Im$, of Carbon Dioxide concentration due to an impulse in CO2 emissions derived from observed time series using the ARX method (solid line). Also shown are the model-derived, normalized impulse response functions corresponding to the three emissions scenarios of of Maier-Reimer and Hasselmann (1987) (broken lines).

Run	Q	pvalue
C(t) vs E(t) only	513.5	0.0000
C(t) vs E(t), C(t-1)	28.5	0.4359
C(t) vs E(t),C(t-1),C(t-2)	28.6	0.3830
C(t) vs E(t) to C(t-3)	24.5	0.5483
C(t) vs E(t) to C(t-4))	24.3	0.5049
C(t) vs E(t) to C(t-5)	22.0	0.5796

Table 3. Ljung-Box parameter, Q, and its probability, P, for five ARX runs of CO_2 concentration, C, vs. global fossil fuel emissions, E. Both time series were decimated by 2.

and the impulse response can be regarded as discretely sampled from a continuous exponential function with time constant given by

$$\tau = -q\Delta t \ln(\hat{\alpha}_1) \tag{9}$$

Substituting $\hat{\alpha}_1$ and its confidence limits into (9)and multiplying by ln(2) gives a half-time of 43 years with confidence limits of 24 years and 193 years. The normalized impulse response is shown in Figure 3 along with those of Figure 17 of MRH.

The sensitivity estimate, S, was 6.77 p.p.m.$GtCO_2^{-1}$.year with 95 percent, t-test confidence limits of 4.03 and 20.15 p.p.m.$GtCO_2^{-1}$.year. The probability that $S > 10^5$ was 0.012 whereas that of MRH is infinite.

4 Discussion

Month by month variations in atmospheric carbon dioxide concentrations from natural causes mask any variation from the recent COVID-19 lock-down. Such rapid variations are due to the absorption and out-gassing of CO_2 by the mixed layer of the ocean as it is warmed and cooled by fluctuating weather systems such as El Niño.

At longer time scales, the response of the carbon dioxide concentration in the atmosphere to a perturbation in production rate is governed by a first order differential equation. Hence variations over time are smoothed by the convolution of the perturbation with the impulse response curve characterised by that equation. The impulse response curve is exponential with a half-time of 43 years and zero remnant fraction. A perturbation in production rate such as the Covid-19 Lock-down would need to last for a comparable time in order to be detectable as a change in concentration.

The precise fit of the regression line in Figure 2 is in sharp contrast to the noisiness of the monthly rates of change shown Figure 1. This apparent contradiction is resolved when we consider the mixed layer Kraus and Turner (1967). The mixed layer is a turbulent layer in which winds and waves have homogenized temperature and chemistry down to some depth which varies between about 10m and 200m. Wind stress increases the depth while solar radiation in calm conditions renews stratification. Because of its turbulent nature, the mixed layer is in intimate contact with the atmosphere, so that heat and soluble gases exchange rapidly between the two reservoirs. The highly stratified thermocline lies below the mixed layer. Apart from regions of upwelling and downwelling, heat and dissolved substances are transferred through the thermocline to and from the deep ocean by diffusion.

In effect then, there are three reservoirs: the atmosphere, the mixed layer and the deep ocean. At time scales of months, exchange of CO_2 between the mixed layer and the atmosphere predominate whereas at time scales of years to decades, the exchange of CO_2

between the deep ocean and the mixed layer predominates. At these longer time scales the mixed layer and atmosphere can be regarded as a single reservoir. The rapid variations in temperature seen in Figure 1**d** only involve the atmosphere and the mixed layer. On the other hand the variation in $\Delta^{14}CO_2$ of Figure 2 is the result of the much slower rate of diffusion of $^{14}CO_2$ from the atmosphere/mixed layer reservoir into the deep ocean.

The impulse response and sensitivity of CO_2 concentration estimated statistically are quite different from conventionally accepted values. The impulse response has an exponential decay with no significant remnant fraction. A possible explanation is the following: the deep ocean is bounded by a turbulent mixed layer and by the highly turbulent Antarctic Circumpolar Current and will therefore be internally mixed by a Kolmogorov cascade of turbulent eddies, some with spatial scales as large as ocean basins and with time scales of, perhaps, decades. Turbulence is a stochastic phenomenon which is difficult to observe at large spatial and temporal scales and which cannot be readily emulated by deterministic models. The complexity of the eddy transports noted by Kamenkovich et al. (2021) calls for reconsideration of how they are estimated in practice, particularly in general circulation models. Eddy diffusion generated by such eddy transports would greatly increase the capacity of the deep ocean to absorb carbon dioxide and so would account for the shorter half time of the observed impulse response of atmospheric CO_2 concentration. Whatever the explanation, there is no observational evidence for the long half times and remnant component of atmospheric CO_2 concentration presently assumed by most modellers.

5 Open Research

Software and data used in the preparation of this article are available for download at Zenodo under the heading *Flawed Carbon Cycle Models*: DOI: 10.5281/zenodo.6302014 (`https://zenodo.org/record/6302014#.YhwtrjpxXct`)

References

Boden, T. A., G. Marland, and R. J. Andres (2017). Global, regional, and national fossil-fuel CO2 emissions. *Carbon Dioxide Information Analysis Center, Oak Ridge National Laboratory, U.S. Department of Energy, Oak Ridge, Tenn., U.S.A.*

Box, G. E. P. and G. Jenkins (1976). *Time Series Analysis: Forecasting and Control.* San Francisco, CA: Holden-Day.

Dengler, J. and J. Reid (2023). Emissions and CO2 concentration—an evidence based approach. *Atmosphere 14*(3), 566.

Ganachaud, A. and C. Wunsch (2000). Improved estimates of global ocean circulation, heat transport and mixingfrom hydrographic data. *Nature 408*, 453–457.

Granger, C. W. J. (1969). Investigating causal relations by econometric models and cross-spectral methods. *Econometrica 37*, 424–438.

Greene, W. H. (2003). *Econometric Analysis (5th ed.)*. New Jersey: Prentice Hall.

Hamilton, E. J. (1994). *Time Series Analysis*. Princeton, New Jersey: Princeton University Press.

Houghton, J. T., Y. Ding, D. J. Griggs, M. Noguer, P. J. van der Linden, X. Dai, K. Maskell, and C. A. Johnson (2001). *IPCC, 2001: climate change 2001: the scientific basis. Contribution of Working Group 1 to the Third Assessment Report of the Intergovernmental Panel on Climate Change*. London: Cambridge University Press.

Kamenkovich, I., P. Berloff, M. Haigh, L. Sun, and Y. Lu (2021). Complexity of mesoscale eddy diffusivity in the ocean. *Geophysical Research Letters 48*(5), e2020GL091719. e2020GL091719 2020GL091719.

Keeling, R., S. Piper, A. Bollenbacher, and J. Walker (2009). Atmospheric CO2 records from sites in the sio air sampling network. In *Trends: A Compendium of Data on Global Change.* Oak Ridge National Laboratory, U.S. Department of Energy, Oak Ridge, Tenn., U.S.A.: Carbon Dioxide Information Analysis Center. Data downloaded from https://www.esrl.noaa.gov/gmd/ccgg/trends/data.html, July 2020.

Kraus, E. and J. Turner (1967). A one-dimensional model of the seasonal thermocline ii. the general theory and its consequences. *Tellus 19*(1), 98–106.

Le Quéré, C., R. Jackson, M. Jones, A. Smith, and S. Abernethy (2020). Temporary reduction in daily CO2 emissions during the covid-19 forced confinement. *Nat. Clim. Chang. 10*, 647–653.

Ljung, G. M. and G. E. P. Box (1978). On a measure of a lack of fit in time series models. *Biometrika 65*, 297–303.

Maier-Reimer, E. and K. Hasselmann (1987). Transport and storage of CO2 in the ocean - an inorganic ocean-circulation carbon cycle model. *Climate Dynamics 2*, 63–90.

Meinshausen, M., E. Vogel, A. Nauels, and K. Lorbacher (2017). Historical greenhouse gas concentrations for climate modelling (cmip6). *Geosci. Model Dev. 10*, 2057–2116. `https://www.climatecollege.unimelb.edu.au/cmip6`.

Nydal, R. and K. Lövseth (1983). Tracing bomb 14 c in the atmosphere, 1962-1980. *Journal of Geophysical Research 88*, 3621–42.

Redfield, A. (1934). On the proportions of organic derivatives in sea water and their relation to the composition of plankton. *James Johnstone Memorial Volume 176*, 176–192. Downloaded 19/7/2020.

Siegenthaler, U. and F. Joos (1992). Use of a simple model for studying ocean tracer distributions and the global carbon cycle. *Tellus 44B*(3), 186–207.

Trenberth, K. E. (1997, 12). The definition of el niño. *Bulletin of the American Meteorological Society 78*(12), 2771–2778.

Zeebe, R. E. (2011, May). On the molecular diffusion coefficients of dissolved CO,HCO3-, and CO32- and their dependence on isotopic mass. *Geochimica et Cosmochimica Acta 75*(9), 2483–2498.

Appendix A Estimating the Impulse Response via the ARX Method

For notational convenience, in the following, all sample means have been removed and random variables are assumed to have zero mean.

The autoregressive moving average method with a single exogenous variable, ARMAX(p,q), is given at time, i, by:

$$Y_i = \alpha_0 x_i + \sum_{j=1}^{p} \alpha_j . y_{i-j} + \sum_{k=1}^{q} \beta_j \Xi_{i-k} \quad , \quad i = 1, ..., N \tag{A1}$$

where the dependent random variable is Y_i, x_i is the exogenous variable, the y_i are past values of Y_i and the Ξ_i are unselfcorrelated random variables with zero mean. The regression coefficients α_0, α_j and β_j are estimated from the data and p and q are small positive integers. The notation is intended to make a clear distinction between random variables which are upper case, and constants, such as past values of random variables, which are lower case. Equation (A1) is a state space representation Hamilton (1994) describing states of the system at a succession of discrete instants; the random variable, Y_i, at one instant becomes the constant, y_i, in the following instant. The direction of time is important in regression, which, unlike correlation, allows causality to be inferred (Granger, 1969).

There are software packages for parameter estimation available under the aegis of the major programming languages. Unfortunately some of these are flawed, because they

estimate the exogenous parameter, α_0, prior to estimating the other parameters, leading to omitted-variable bias (Greene, 2003); all parameters must be estimated simultaneously in a regression model.

Estimation of the MA coefficients, $\{\beta_i\}$, requires an iterative Kalman filter method which may not converge. The second, moving average summation in (A1), describes a convoluting or "blurring" function, so that $q > 1$ when the sampling interval, Δt, is too small. Estimation of the MA coefficients can be avoided by decimating the time series by q to give a new time series with a larger sampling interval, $q\Delta t$, for which the innovation sequence, $\{\Xi_m\}$, is unselfcorrelated. Then (A1) becomes

$$Y_m = \alpha_0 x_m + \sum_{n=1}^{p} \alpha_n . y_{m-n} + \Xi_m \quad , \quad m = 1, ..., M \tag{A2}$$

where $m = qi$, $qM \leq N$, The model summarized by (A2) is an ARX(p) model for 'autoregressive with exogenous variable'. The regression coefficients, α_i, and their confidence limits are estimated using Ordinary Least Squares. The sequence of residuals, $\{\xi_m\}$, is given by

$$\xi_m = y_m - \left(\hat{\alpha}_0 x_m + \sum_{n=1}^{p} \hat{\alpha}_n . y_{m-n} \right) \quad , \quad m = 1, ..., M \tag{A3}$$

where y_m is the sample value or 'realization' of Y_m and $\hat{\alpha}_0$ to $\hat{\alpha}_p$ are the regression coefficient estimates. The $\{\xi_m\}$ are tested using the Q statistic with probability P (Ljung and Box, 1978). The minimum number of coefficients, $\hat{p}$, is found for which P is greater than some confidence level, say 0.1, for which it can be assumed the innovation sequence is not self-correlated.

Our best estimate of the relationship between the two time series is then

$$\sum_{n=0}^{\hat{p}} \hat{\gamma}_n y_{m-n} = \hat{\alpha}_0 x_m \tag{A4}$$

where

$$\hat{\gamma}_0 = 1 \tag{A5}$$

and

$$\hat{\gamma}_n = -\hat{\alpha}_n \quad , \quad n = 1, ..., \hat{p} \tag{A6}$$

The sequence $\{\gamma_n\}$ specified by (A4) is the prediction error filter of the autoregressive process.

We can define a time series more precisely as a finite or semi-infinite sequence, $\{x_0, x_1, x_2, ...\}$ for which the index specifies successive equally spaced intervals of time. The convolution, $c = \{c_k; k = 0, 1, ..., r\} = a * b$, of two time series $a = \{a_i; i = 0, 1, ..., p-1\}$ and $b = \{b_j; j = 0, 1, ..., q\}$, is defined by

$$c_k = \sum_{i+j=k} a_i b_j \tag{A7}$$

Under this definition convolution satisfies the commutative, associative and distributive laws of arithmetic. Note also that

$$\sum_i a_i \cdot \sum_j b_j = \sum_k \sum_{i+j=k} a_i b_j = \sum_k c_k \tag{A8}$$

The sum on the left hand side of (A4) is a convolution and (A4) can be written

$$\hat{\gamma} * y = \hat{\alpha}_0 x \tag{A9}$$

A more useful form of (A9) is

$$y = \hat{I} * x \tag{A10}$$

where $\hat{I}$ is the convolutional reciprocal of $\hat{\gamma}/\hat{\alpha}_0$ given by

$$\hat{I} * \hat{\gamma} = \hat{\alpha}_0\{1\} \tag{A11}$$

and is termed the impulse response. It can be estimated numerically by iteration using (A11) in the form

$$\hat{I}_m = \sum_{i=1}^{p} \hat{\alpha}_i \hat{I}_{m-i} + \hat{\alpha}_0 \delta_m \tag{A12}$$

For display purposes and inter-comparison a normalized impulse response, $\Im$, may be used where

$$\Im * \gamma = \{1\} \tag{A13}$$

Thus the normalized impulse response is the convolutional inverse of the prediction error filter of the autoregressive process.

Like the regression coefficients, I is a property of the system under investigation and $\hat{I}$ is its estimate. Equation (A10) describes the output of the system, y, in response to *any* input sequence, x.

The sensitivity of the system, S, is defined here as the response at infinity to a unit step function, H_j, where $H_j = 0$ for $j < 0$ and $H_j = 1$ for $j \geq 0$. From (A7)

$$S = \lim_{k\to\infty} S_k = \lim_{k\to\infty} \sum_{i+j=k} I_i H_j = \sum_{k=0}^{\infty} I_k \tag{A14}$$

i.e. it is the sum of the terms of the impulse response. It is a random variable on which confidence limits can be placed.

According to (A8) the sum of a convolution is equal to the product of the sums of the convoluting factors. Thus, from (A11)

$$\sum_{m=0}^{\infty} I_m \sum_{n=0}^{p} \gamma_n = S \sum_{n=0}^{p} \gamma_n = \alpha_0 \tag{A15}$$

from which $\hat{S}$ can be estimated in terms of the prediction error filter, $\{\hat{\gamma}_n\}$.